

PAPER

Dark–dark soliton breathing patterns in multi-component Bose–Einstein condensates

To cite this article: Wenlong Wang *et al* 2021 *J. Phys. B: At. Mol. Opt. Phys.* **54** 055301

View the [article online](#) for updates and enhancements.






IOP | ebooks™

Bringing together innovative digital publishing with leading authors from the global scientific community.

Start exploring the collection—download the first chapter of every title for free.

Dark–dark soliton breathing patterns in multi-component Bose–Einstein condensates

Wenlong Wang^{1,*} , Li-Chen Zhao^{2,3}, Efstathios G Charalampidis⁴  and Panayotis G Kevrekidis^{5,6} 

¹ College of Physics, Sichuan University, Chengdu 610065, People's Republic of China

² School of Physics, Northwest University, Xi'an 710069, People's Republic of China

³ Shaanxi Key Laboratory for Theoretical Physics Frontiers, Xi'an 710069, People's Republic of China

⁴ Mathematics Department, California Polytechnic State University, San Luis Obispo, CA 93407-0403, United States of America

⁵ Department of Mathematics and Statistics, University of Massachusetts, Amherst, MA 01003-4515, United States of America

⁶ Mathematical Institute, University of Oxford, Oxford, United Kingdom

E-mail: wenlongcmp@scu.edu.cn, zhaolichen3@nwu.edu.cn, echarala@calpoly.edu and kevrekid@math.umass.edu

Received 28 October 2020, revised 7 January 2021

Accepted for publication 15 February 2021

Published 2 April 2021



CrossMark

Abstract

In this work, we explore systematically various $SO(2)$ -rotation-induced multiple dark–dark (DD) soliton breathing patterns obtained from stationary and spectrally stable multiple dark–bright (DB) and DD waveforms in trapped one-dimensional, two-component atomic Bose–Einstein condensates. The stationary states stemming from the associated linear limits (as the eigenfunctions of the quantum harmonic oscillator problem) are parametrically continued to the nonlinear regimes by varying the respective chemical potentials, i.e. from the low-density linear limits to the high-density Thomas–Fermi (TF) regimes. We perform a Bogolyubov–de Gennes spectral stability analysis to identify stable parametric regimes of these states, finding a wide range of stability intervals in the TF regimes for all of the states considered herein. Upon applying an $SO(2)$ -rotation to stable steady states, one-, two-, three-, four-, and many DD soliton breathing patterns are observed in the numerical simulations. Furthermore, analytic solutions up to three DB solitons in the homogeneous setting, and three-component systems are also investigated.

Keywords: dark–dark solitons, dark–bright solitons, solitary waves, Bose–Einstein condensates, multicomponent condensates

(Some figures may appear in colour only in the online journal)

1. Introduction

Bose–Einstein condensates (BECs) have attracted a significant amount of attention over more than two decades for investigating macroscopic quantum phenomena [1, 2]. One major theme of research concerns (effectively) nonlinear coherent structure solutions in the form of solitary waves that are supported by

these quantum gases [3], which share many similarities with nonlinear optics [4]. A large variety of solitary waves has been studied in the context of BECs, ranging from bright solitons in attractive condensates [5] to dark solitons [6], vortices [7], and vortical filaments as well as rings [8–10] in repulsive condensates.

One important extension of these studies is the investigation of multicomponent condensates supporting, e.g. dark–bright (DB), dark–dark (DD), dark–antidark (DAD) structures in

* Author to whom any correspondence should be addressed.

repulsive condensates [11–15]; see, e.g. [16], for a relatively recent review summarizing some of the early work on the subject both in atomic physics, as well as in nonlinear optics. It should be noted in passing that the bright soliton cannot be sustained on its own in a single repulsive condensate but exists as a result of the effective trapping of the dark soliton in the other component. It is also relevant to mention that the study of such structures has motivated extensions thereof also in higher dimensions [17–19]. In recent years, there has been a significant number of further efforts to extend this multi-component understanding to a variety of more complex settings, including, e.g. the one of three-component condensates [20], that of magnetic solitons in both binary [21] and even spinor [22] BECs, and very recently the examination of multiple DAD states in two-component systems [23].

Our primary focus herein will be more concretely on the two-component setting. In this case and when only incoherent coupling between the components is involved, the system trivially supports the $U(1) \times U(1)$ symmetry. In the special Manakov case [24], in which all the intra- and inter-component interaction strengths are equal, there is an additional $SU(2)$ symmetry [25]; see the next section for details. One particularly interesting result is that this $SU(2)$ -symmetry can induce the formation of the so-called DD breathing or beating dynamics upon rotating stationary and stable DB soliton solutions [26]. This rotation has been exploited to produce single DD states from corresponding single DB ones, and these DD states have been studied in various (both one- and higher-dimensional) settings [17, 19, 26–28]. In the integrable Manakov case, generalized N -soliton states in the form of DD states can be obtained leveraging techniques from integrability [29, 30]. Here, on the other hand, we will focus on multiple-wave patterns obtained from the linear limit of the quantum harmonic oscillator. These states can be generalized to DB soliton crystal states bearing arbitrary many DBs [31]. Note that in the present work, we are primarily interested in stable patterns, looking for stable DB solitons, although the symmetry is not limited to stable structures or even stationary states.

Given the above state of the field, the main purpose of the present work is to offer a systematic study of multiple DB solitons or more precisely DB and DD mixtures, and their associated stable multiple DD soliton breathing patterns via an $SU(2)$ rotation. Even more, the recent experimental developments enabling both the sequential and alternating seeding of dark and antidark structures in the two components [23] suggest that this direction is especially timely and worthwhile to study. Additionally, two further and more recent experiments have since appeared indicating the tremendous control presently available at the level of creation of patterns with phase windings, such as dark solitary waves. The first one in single-component condensates illustrated how to leverage *both* amplitude and phase engineering in order to controllably produce dark solitary waves of any accessible (within this family of solutions) speed [32]. The second leveraged a spatially localized spin rotation realized with a steerable laser beam in order to generate *multiple* dark–bright–bright (vector) solitons with a high degree of experimental control so as to examine their collisions at different relative phases [33]. Moreover,

the latter work represents the first experimental realization of a system very close to the three-component vector Manakov model, considered herein, due to the operation of the experiment in a regime where the spin-dependent effects are significantly suppressed. The above experimental developments pave the way for the more complex, yet potentially dynamically robust multiple-winding patterns presented in what follows.

We focus on the case of a 1D two-component condensate confined in a harmonic trap. A key feature of our study is that we explore these structures systematically from the low-density linear limits to the high-density Thomas–Fermi (TF) regimes, and their Bogolyubov–de Gennes (BdG) spectra are computed in the realm of spectral stability analysis. These computations shed light on potentially stable parametric regimes in the chemical potentials in which bound modes are long lived ones (and observed in our simulations). Such a methodology can be utilized to construct a whole series of topologically distinct stationary states. To that end, a component with $n > 0$ solitons stemming from the quantum harmonic oscillator eigenfunction $|n\rangle$ is progressively coupled to $m = 0, 1, \dots, n-1$ solitons in the other component stemming from the state $|m\rangle$. These states are therefore expected to exist as the two components decouple in the low-density linear limits. We assume (without loss of generality) $n > m \geq 0$ and refer to the composite structure as state S_{nm} , where S stands for both state and soliton. For each integer n , there is a total of n *distinct* stationary states; so that n also corresponds to the number of distinct DD breathing patterns. Note that this enumeration accounts for the (definite parity) states with $m = 0, \dots, n-1$, and is relevant in the vicinity of the linear limit. In principle, this does not preclude the potential of other (asymmetric) states to arise in regimes of high nonlinearity, without persisting all the way to the linear limit. Therefore, the number of patterns grows rapidly for these composite structures. For example, up to $n = 4$, there exist 10 breathing patterns; in general, for given n , the number of breathing patterns is $n(n+1)/2$. In the specific case of $n = 2$, our procedure automatically reproduces both the in-phase (coupled with $m = 0$) and the out-of-phase (coupled with $m = 1$) DB solitons, resulting (upon rotation) in their corresponding DD breathing patterns [26].

It is straightforward to see that in S_{n0} the bright solitary waves are all in phase as the second component is uniform in phase, while in $S_{n,n-1}$ (here a comma is added for clarity) the bright ones are fully out of phase as the roots of neighboring orthogonal polynomials alternate [34]. Interestingly, the fully in-phase DB will produce, upon rotation, an out-of-phase DD breathing pattern, as each of the DB solitary waves converts into a DD one. As m grows from 0 to $n-1$, the number of dark solitons in the second component increases by one successively, and the resulting rotated patterns will convert each of the DBs into a DD, while collocated zero crossings will be preserved under the transformation. The breathing patterns are, in fact, reminiscent of a 1D mass-spring system with fixed boundary conditions, and for n masses, there are n normal modes increasingly out of phase. See figure 1 for a schematic diagram of the S_{4m} states and an explanation of how they are modified upon rotation.

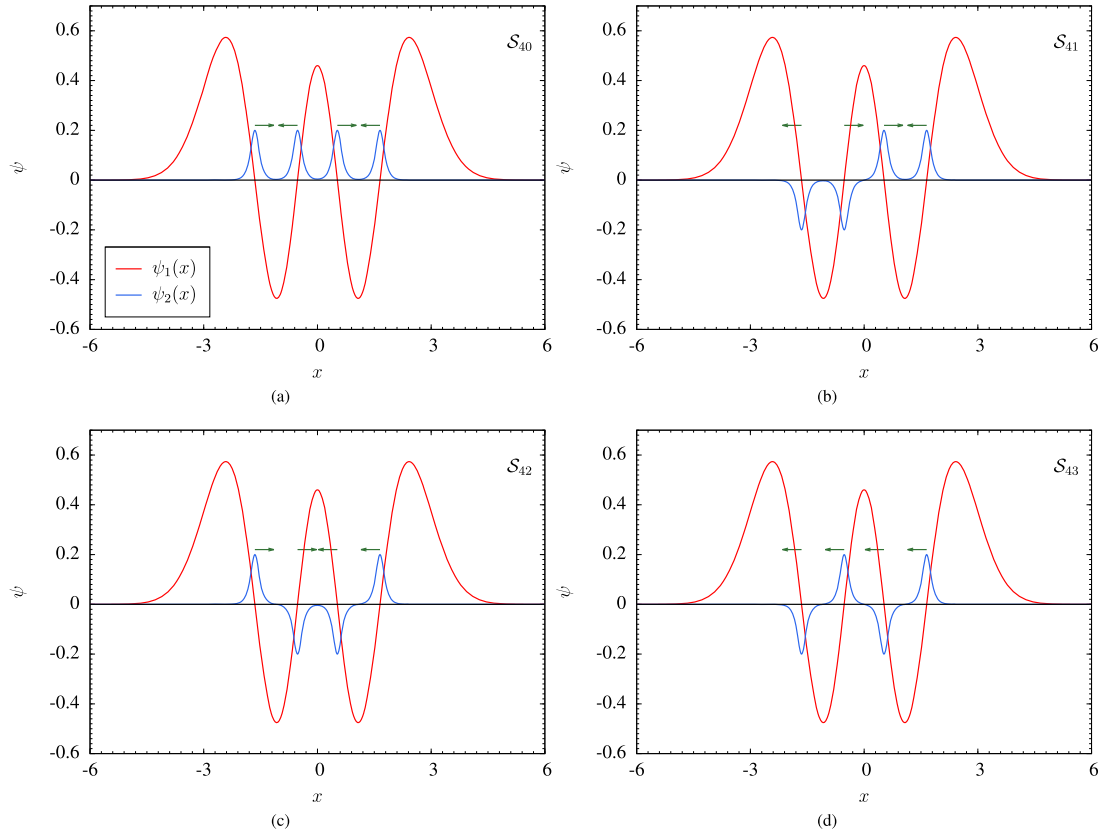


Figure 1. Schematic diagram showing the mixing of various topologically distinct states can cause the dark solitons (nodes of ψ_1) to shift in different directions. Here, the \mathcal{S}_{4m} states are shown. The arrows indicate how the corresponding dark soliton positions shift upon adding the bright field, as a result of an SO(2) rotation (with $\delta = \pi/4$ below); when subtracting, the arrows flip to the opposite direction instead. It is observed that as the number of nodes m increases in the second component, the shifting of the dark solitons in the first component becomes increasingly in phase. See figure 4 for numerically exact field configurations and the resulting DD beating patterns.

In this work, we explore all the distinct states up to $n = 4$. For higher n , the computation gets increasingly tedious as well as more expensive. One reason is that the number of combinations grows with n as mentioned above, and importantly so does the number of unstable modes of the states. This behavior is strongly reminiscent of the one-component counterpart of dark soliton clusters, where a state containing more dark solitons requires a larger chemical potential (or atomic density) to get stabilized [35]. Indeed, as is discussed also in [16], the larger number of windings leads to a higher number of unstable eigendirections; these are chiefly unstable due to resonances in the vicinity of the linear limit, but progressively lead to fewer and further between resonances/instabilities as the chemical potentials become larger. This, in turn, necessitates higher chemical potentials (or densities) in order to stabilize the configurations compared with the low-lying structures. In order to reach large chemical potentials, both a larger domain (to ensure that the patterns identified are located comfortably within the condensate) and a finer spacing (to accurately resolve the solitonic structures) are required to achieve high accuracy in numerical computations. For higher n , we examine only the state \mathcal{S}_{n0} which typically has a wider region of stability (in chemical potentials) among the different values of m . In this work, we have explored the cases with $n = 5, 6, \dots$, up to 10, thus forming a DB ‘mini-lattice’. In fact, our results

involve quite substantial computations, despite our work being restricted to 1D: for example, to stabilize the $\mathcal{S}_{10,0}$ structure, we have to reach chemical potentials on the order of 100.

In addition to breathing patterns in a harmonic trap, we discuss the homogeneous setting with up to three soliton structures (and the states that emerge from their rotation); finally, we extend our considerations to three-component systems. In the former case, we are interested in exact solutions of bound DB solitons and the corresponding DD breathing waveforms. In the latter case, the number of stationary states is even higher due to the different combinations of the pertinent eigenstates. For clarity in this case, we introduce the shorthand notation \mathcal{S}_{mnp} ($m > n > p \geq 0$) which stems itself from the coupling of the harmonic oscillator states $|m\rangle$, $|n\rangle$, and $|p\rangle$. We shall not explore all of these structures in detail in this work, but rather our goal is to illustrate prototypical examples involving them and demonstrate the applicability of our current approach in tracing states from the linear limits. In the three-component case, we will explore SU(3) rotated breathing patterns, again using stable stationary solitonic structures as a starting point for performing the corresponding rotations.

Our presentation is organized as follows. In section 2, we introduce the model, the SU(2) (and SO(2)) symmetry and the various numerical methods employed in this work. Next, we present our numerical and analytical results in section 3.

Finally, our conclusions and a number of open problems for future consideration are given in section 4.

2. Models and methods

We first present the mean-field Gross–Pitaevskii equation (GPE) and the SU(2) symmetry for a two-component condensate at the Manakov limit. Then, we discuss our methodology for constructing stationary solitons from the linear limits, and the numerical methods employed in the nonlinear realm for identifying stationary states, performing stability analysis, and dynamics. Finally, we briefly describe the analytical method and the generalization to three-component systems.

2.1. Computational setup, dimensional reduction and SU(2) symmetry

In the framework of mean-field theory, and for sufficiently low temperatures, the dynamics of a strongly transversely confined 1D two-component repulsive BEC in a time-independent trap $V = V(x)$, is described by the following coupled dimensionless GPEs [3]:

$$i \frac{\partial \psi_1}{\partial t} = -\frac{1}{2} \frac{\partial^2 \psi_1}{\partial x^2} + V \psi_1 + (g_{11} |\psi_1|^2 + g_{12} |\psi_2|^2) \psi_1, \quad (1a)$$

$$i \frac{\partial \psi_2}{\partial t} = -\frac{1}{2} \frac{\partial^2 \psi_2}{\partial x^2} + V \psi_2 + (g_{21} |\psi_1|^2 + g_{22} |\psi_2|^2) \psi_2, \quad (1b)$$

where $\psi_1 = \psi_1(x, t)$ and $\psi_2 = \psi_2(x, t)$ are two complex scalar macroscopic wavefunctions. In order to study the SU(2)-induced breathing patterns, we consider mainly in this work the Manakov limit $g_{11} = g_{12} = g_{21} = g_{22} = 1$, although effects of weak deviations are also considered in our subsequent discussion. Such effects are encountered, e.g. in the study of hyperfine states of ^{87}Rb [1–3]. The condensates, unless otherwise specified, are confined in a harmonic magnetic trap of the form:

$$V = \frac{1}{2} \omega^2 x^2, \quad (2)$$

where the trapping frequency ω is set (without loss of generality) to $\omega = 1$. Stationary states with chemical potentials μ_1 and μ_2 for the first and second components, respectively, are constructed by considering the Ansätze:

$$\begin{aligned} \psi_1(x, t) &= \psi_1^0(x) e^{-i\mu_1 t}, \\ \psi_2(x, t) &= \psi_2^0(x) e^{-i\mu_2 t}, \end{aligned} \quad (3)$$

which lead to the stationary equations:

$$\begin{aligned} -\frac{1}{2} \frac{d^2 \psi_1^0}{dx^2} + V \psi_1^0 + (|\psi_1^0|^2 + |\psi_2^0|^2) \psi_1^0 &= \mu_1 \psi_1^0, \\ -\frac{1}{2} \frac{d^2 \psi_2^0}{dx^2} + V \psi_2^0 + (|\psi_1^0|^2 + |\psi_2^0|^2) \psi_2^0 &= \mu_2 \psi_2^0. \end{aligned} \quad (4)$$

We briefly outline the dimensional reduction and the subsequent scaling analysis of the dimensional multicomponent GPE here, as we have used an ‘unconventional’ scaling *effectively* setting $\omega = g = 1$. Starting from the

3D GPE in physical units, we first apply the dimensional reduction from 3D to 1D by using the (separation of variables) ansatz $\psi_j(x, y, z, t) = \psi_j(x, t) \phi_0(y, t) \phi_0(z, t)$ and $V = m(\omega_x^2 x^2 + \omega_y^2 y^2 + \omega_z^2 z^2)/2$, where ϕ_0 is the transverse quantum harmonic oscillator ground state. Having this ansatz and the 3D GPE at hand, we take the inner products of the GPE with both $\phi_0(y, t)$ and $\phi_0(z, t)$, thus arriving at an effective one-dimensional GPE (still in physical units). Next, we apply the regular scaling of the quantum harmonic oscillator [36] to set the GPE in a dimensionless form, and a subsequent scaling of the wavefunction in order to set the nonlinearity coefficient to 1, finally yielding equations (1a) and (1b). In summary, our length is measured in units of the axial harmonic oscillator length $\ell_x = \sqrt{\hbar/(m\omega_x)}$, time in units of $1/\omega_x$, and the chemical potential in units of $\hbar\omega_x$. The number of particles in the j th component is $N_j = \frac{1}{g_{1D}} \int |\psi_j|^2 dx$ with $g_{1D} = \frac{2\omega_\perp a_s}{\omega_x \ell_x}$, and a_s stands for the s-wave scattering length. While we cannot obtain N_j analytically, we can estimate the total number of particles in the pertinent TF regime. Indeed, and within the TF radius $\sqrt{2\mu_1}$, the total density profile is approximately $\max(\mu_1 - V(x), 0)$ in our setting which in turn yields $N_{\text{total}} = N_1 + N_2 \approx \frac{2}{3g_{1D}} (\sqrt{2\mu_1})^3$. For example, $\mu_1 = 100$ corresponds to approximately a total of 10^4 atoms which are experimentally accessible. However, the dimensional reduction also requires that $\mu_j \ll g_{1D} \ell_x / (8a_s) = \omega_\perp / (4\omega_x)$ in addition to $\omega_x / \omega_\perp \ll 1$ [3]. In BEC experiments, we have the more experimentally realistic case corresponding to $\omega_x / \omega_\perp \sim 0.01$ with $\ell_x \sim 10^{-6}$ m and $a_s \sim 10^{-9}$ m [23, 37] which in turn suggests $\mu_1 \ll 25$. On the other hand, if $\omega_x / \omega_\perp \sim 0.001$ (representing a setup not-currently-realized, to our knowledge, but plausibly accessible within state-of-the-art BEC settings), it will require $\mu_1 \ll 250$. With the latter choice, and upon using, e.g. $\mu_1 = 150$, one could reach atom numbers of a few thousand atoms which are realistic in dark soliton experiments [38]. As we shall see below, it is straightforward to stabilize low-lying structures, yet the stabilization of more complex ones, e.g. $S_{10,0}$, may be harder to achieve.

We now turn our focus on the U(1) \times U(1) symmetry of the system of equations (1a) and (1b), and additionally its SU(2) symmetry in the Manakov case (where all interaction coefficients are set to unity therein). In particular, if $(\psi_1, \psi_2)^T$ is a solution to the system (1a) and (1b), then $(\psi_1 \exp(i\theta_1), \psi_2 \exp(i\theta_2))^T$ also is, where θ_1 and θ_2 are two real constants. In the Manakov case, it is straightforward to show that

$$\begin{pmatrix} \psi_1' \\ \psi_2' \end{pmatrix} = U \begin{pmatrix} \psi_1 \\ \psi_2 \end{pmatrix} = \begin{pmatrix} \alpha & -\beta^* \\ \beta & \alpha^* \end{pmatrix} \begin{pmatrix} \psi_1 \\ \psi_2 \end{pmatrix}, \quad (5)$$

is also a solution, where $UU^\dagger = \mathbb{I}$, $|\alpha|^2 + |\beta|^2 = 1$, and the star (*) denotes complex conjugation. Note that the total density profile is invariant upon rotation, i.e. $|\psi_1|^2 + |\psi_2|^2 = |\psi_1'|^2 + |\psi_2'|^2$. In this work, we explore the subset of SO(2) rotations:

$$\begin{pmatrix} \psi_1' \\ \psi_2' \end{pmatrix} = \begin{pmatrix} \cos \delta & \sin \delta \\ -\sin \delta & \cos \delta \end{pmatrix} \begin{pmatrix} \psi_1 \\ \psi_2 \end{pmatrix}, \quad (6)$$

and focus on the most symmetric case using $\delta = \pi/4$.

For the two-component case, we identify stationary states by using a finite element method for the spatial discretization and employing Newton's method for the underlying root-finding problem. The linear harmonic oscillator states (which are suitable in the low density limit where the cubic nonlinear terms can be neglected) are used as initial guesses near the respective linear limits. The obtained solutions (upon convergence of Newton's method in this weakly nonlinear regime) are parametrically continued to large chemical potentials by performing a sequential continuation. Since our goal in the present work is to identify stable stationary states, we compute the BdG stability spectrum (see, e.g. [3] for a discussion thereof for the multi-component system) along the (μ_1, μ_2) parametric continuation line considered and select a stable solution which will be rotated subsequently. The interested reader can also find details of the BdG stability matrix in [17]; in short, and given a stationary solution $\psi_j^0(x)$ to the two-component GPE (i.e. $j = 1, 2$), the BdG matrix (and its spectrum) is obtained by introducing the following perturbation Ansätze:

$$\tilde{\psi}_j(x, t) = e^{-i\mu_j t} \left\{ \psi_j^0(x) + \varepsilon \left(a_j(x)e^{\lambda t} + b_j^*(x)e^{\lambda^* t} \right) \right\}, \quad j = 1, 2, \quad (7)$$

where $\varepsilon \ll 1$. The eigenvalues λ with $\lambda = \lambda_r + i\lambda_i$ of the resulting BdG matrix (see [17]) determine whether a solution is (spectrally) stable or not. In particular, if all $\lambda_r = 0$, then a solution is deemed stable; otherwise it is unstable. Our dynamics of either the original stationary states or of the rotated (and expected to be breathing) ones is performed by using the standard fourth-order Runge–Kutta method.

The analytical multiple DB soliton solutions and the rotation thereof for the homogeneous setting [39] are also used in order to produce breathing states. In this work, we discuss the two and three DB soliton states, and then their corresponding rotated breathing patterns. It is worth noting that these solutions generally cannot be tuned to be fully stationary, despite the fact that they can be approximately stationary when multiple solitons are well separated. This can also be understood intuitively (as in the trapped case discussed above) since the stationarity stems from the interplay between the pairwise interaction of the DB structures and the restoring effect of the trap on each of the waves [11]. For homogeneous settings, the absence of the latter does not allow an equilibrium configuration given the absence of a counterbalance for the former. Nevertheless, the SO(2) rotation and symmetry is not limited to stationary states, and applies to these dynamic cases as well. Consequently, several time scales can manifest themselves in the dynamics, in contrast to the periodic solutions rotated from stationary states.

The computational setup for the three-component system is similar to that of the two-component case. The pertinent equation of motion and the corresponding BdG stability matrix will be presented in section 3.2 and appendix B, respectively. It should be noted in passing that the same form of the perturbation Ansätze of equation (7) is used for investigating the BdG spectrum in the three-component system but now with $j = 1, 2, 3$. In this system, there are three chemical

potentials, extending from the linear limits to the TF regimes in the (μ_1, μ_2, μ_3) parameter space. In this work, we investigate the states \mathcal{S}_{210} and \mathcal{S}_{310} , including their existence, stability, and SU(3)-induced breathing dynamics. Here, it is important to comment on the nature of the corresponding model. It is well-known that the spinor condensate mean-field model [40, 41] that has recently been explored also experimentally for various solitonic configurations [20, 22] is nontrivially different from the Manakov model. In particular, the latter contains only the spin-independent part of the hyperfine state interactions, while the former contains also the spin-dependent part coupling the phases of the different components [40, 41]. Here, motivated also by multi-component nonlinear optical problems [25], we restrict our considerations to the Manakov case, however, we note that a more detailed consideration of the spin-dependent effect on these states would be of interest in its own right.

2.2. Constructing irreducible topologically distinct stationary states from the linear limits

It is known that a rotated single DB soliton (formed by the coupling of a $|1\rangle$ state with a $|0\rangle$ one) produces a DD breathing state, and has been extensively studied (see, [26, 27]). However, there are two cases for two DB solitons [42]: (a) the in-phase case where the bright peaks have the same phase and (b) the out-of-phase case where the bright peaks have the opposite phase. These solitons (in the linear limit) involve the coupling of the $|2\rangle$ state in the first component with the $|0\rangle$ state and the $|1\rangle$ state in the second component, respectively [31]. Those states can be continued to the high density regimes in the (μ_1, μ_2) parameter space. In our work, we take a simple linear trajectory from the linear limit to a final high-density regime. Because of the linear trajectory, we can only refer to μ_1 for simplicity if the respective initial and final chemical potentials $\bar{\mu}_i$ and $\bar{\mu}_f$ are given due to the constraint $\bar{\mu} = \bar{\mu}_i + \epsilon(\bar{\mu}_f - \bar{\mu}_i)$, $\epsilon \in (0, 1]$. For a given μ_1 , one can calculate the parameter ϵ , and then μ_j , for $j \neq 1$. Consequently in what follows, we will present the BdG analysis results as a function of μ_1 . These states are conveniently labeled as \mathcal{S}_{10} , \mathcal{S}_{20} , and \mathcal{S}_{21} in the above notation, respectively.

These considerations can be generalized to any pair of harmonic oscillator states. Specifically, the state $|n\rangle$ can be coupled successively with the $|m\rangle$ state, thus forming the \mathcal{S}_{nm} state with $m = 0, 1, 2, \dots, n-1$. It should be noted that not all of these structures are DB solitons. For example, the state \mathcal{S}_{31} has three dark solitons in the first component but with only two out-of-phase bright peaks at the sides, in the second component. Between these peaks, naturally per the anti-symmetric nature of the $m = 1$ state lies a dark solitonic structure in the second component. Therefore, the state \mathcal{S}_{31} is a stationary state concatenating a DB wave on the one end, with a DD one in the middle and a DB structure on the other end. It is noted in passing that the DD structure is expected to exist whenever both n and m are odd. Finally, for each integer n , there is a total of n distinct stationary states and corresponding breathing patterns *stemming from the linear limit*; this is noted because in principle states that do not terminate at the linear limit may exist in the highly nonlinear regime.

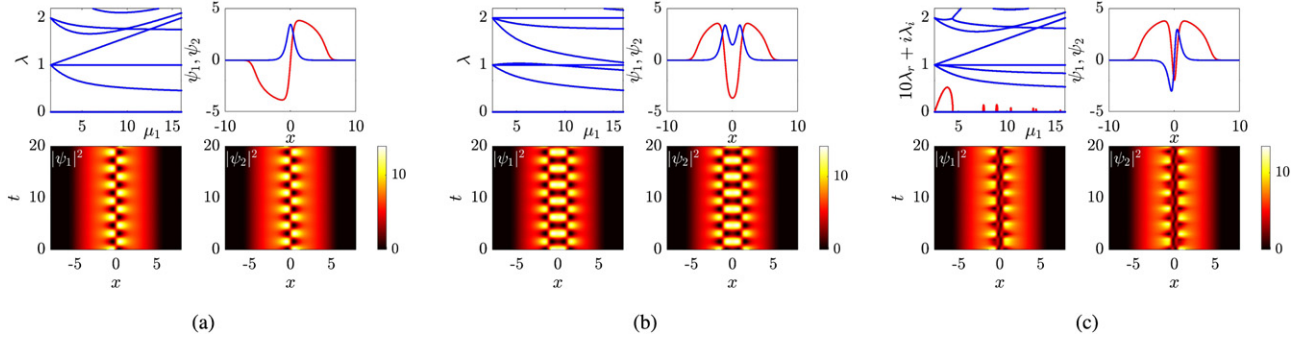


Figure 2. Panel (a): the BdG spectrum ($\lambda = \lambda_r + i\lambda_i$) of the DB soliton along a linear trajectory from the linear limit (1.5, 0.5) to a typical large-density limit (16, 14) in the (μ_1, μ_2) parameter space. Note that the spectrum is shown as a function of μ_1 only because of the linear trajectory constraint. Red and blue curves denote unstable (real parts of eigenvalues λ_r in red) and stable (imaginary parts of eigenvalues λ_i in blue) modes, respectively. Here, the DB spectrum is entirely imaginary. The stationary DB profile at the end of the parametric line is illustrated, along with the induced DD oscillating patterns, i.e. the DB pattern is SO(2)-rotated and fed into the time evolution dynamics in order to observe this dynamical phenomenology. Here and in the contour plots that will follow throughout the manuscript, the density $(|\psi_i|^2, i = 1, 2)$ will be shown for the different components as a function of space and time. The DB, as well as its rotated variant are fully stable and robust. Panels (b) and (c): same as (a) but for the S_{2m} family from the linear limit (2.5, $m + 0.5$) to a typical large-density limit (16, 14). The bright solitons are in phase for $m = 0$ (b) and out of phase for $m = 1$ (c), the in-phase two-DB state is fully stable, but the out-of-phase one has several (here seven) weak instability peaks. Note that the real part of the eigenvalues for S_{21} is enlarged by a factor of 10 for visualization purposes, i.e. we have plotted $10\lambda_r$ and λ_i in this spectrum and the maximum growth rate is approximately $0.5/10 = 0.05$. All of the breathing patterns in this work are integrated and found to be robust up to $t = 1000$.

We have omitted the structures stemming from the same linear states, i.e. S_{mn} with $m = n$. Although they are topologically distinct ones, they require same chemical potentials in the two components due to the fact that from equation (4), one can derive the condition $\langle \psi_1^0 | \psi_2^0 \rangle (\mu_1 - \mu_2) = 0$. In other words, if the two fields are not orthogonal, they must have the same chemical potential. This strongly suggests that the two field profiles in S_{mn} are identical up to a scaling factor, which is numerically confirmed. Consequently, such a state can be viewed as a splitting of the corresponding single-component state. If ψ_{1D} is a stationary state of the one-component system, then $(\cos(\delta)\psi_{1D}, \sin(\delta)\psi_{1D})^T$ is a solution of the two-component system with the same interaction strengths. The action of rotation matrices as considered above will, thus, not produce genuinely new states in this case. Therefore, we focus on states of distinct quantum numbers, both for the two-component but also for the following three-component system. In a sense, we investigate all the *irreducible* topologically distinct states. The construction can be further generalized to the three-component system, where state S_{mnp} is expected to be formed by coupling the harmonic oscillator states $|m\rangle$, $|n\rangle$, and $|p\rangle$, where $m > n > p \geq 0$. In this work, for proof-of-principle purposes, we only explore two specific yet typical low-lying states S_{210} and S_{310} , focusing on their existence, stability, and the SU(3)-induced breathing patterns.

3. Results

3.1. Multiple dark-dark breathing patterns in two components

The single DB soliton appears to be very robust and is found to be fully stable over the parameter ranges considered, as illustrated in the left panel of figure 2. The same is true for the two DB solitons in phase (see the middle panel of the figure). On

the other hand, the two DB solitons out of phase encounter a series of instabilities, a total of seven unstable peaks along the parametric line. These instabilities are in line with what is known about both multiple dark solitons (in one-component condensates) [3] and also about multiple DB and even DAD solitary waves in two-component condensates; for a recent discussion, see, e.g. [23]. In particular, a so-called negative Krein (or energy) signature mode associated with the out-of-phase vibration of the two DB solitary waves becomes resonant with modes of the background cloud sequentially. The first of these resonances in the vicinity of $\lambda_i = 2$ can be observed in the right panel of figure 2 (this also corresponds to the largest instability (red) ‘bubble’). However, most of the peaks are rather narrow and all of the peaks are rather weak, i.e. they correspond to low growth rates of the associated instability. Note that the real part of the eigenvalues is enlarged by a factor of 10 for ease of visualization, i.e. the maximum growth rate is only about $0.5/10 = 0.05$. Therefore, there are wide intervals of stability for these low-lying states. It is interesting that the DD breathing patterns involve the conversion of each of the DB structures into a DD, creating new phase alternations (e.g. in the bright component) as a consequence of the emergence of the DD states.

Next, we focus on the S_{3m} family as shown in figure 3. In this family, all the states considered bear unstable modes; in fact all the states have *at least* three potentially unstable modes because of $n = 3$. Furthermore, the number of potential instabilities grows with m . In this context, it is reasonable to expect that for states S_{nm} , the maximal number of potentially unstable eigendirections is $n + m$. However, it is important to emphasize that there are again wide ranges of stability. The associated instability bubbles will bear quite small growth rates, with the exception of the first one associated with resonances emerging for small chemical potentials (particle numbers) right off of the linear limit. From a structural

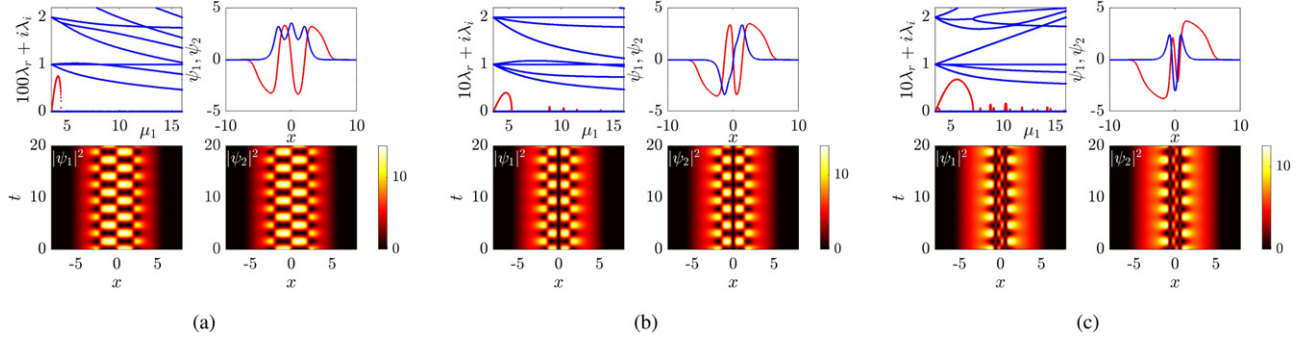


Figure 3. Same as figure 2, but for the \mathcal{S}_{3m} family of $m = 0$ (a), $m = 1$ (b), and $m = 2$ (c) from the linear limits $(3.5, m + 0.5)$ to a typical large-density limit $(16, 14)$ in the (μ_1, μ_2) parameter space. Here, even the in-phase state has an unstable mode, although it is rather weak. The states get progressively more unstable as m increases, i.e. as the number of dark soliton increases in the second component. Note that the second state \mathcal{S}_{31} consists of a DB (left end), DD (middle), and DB (right end) structure.

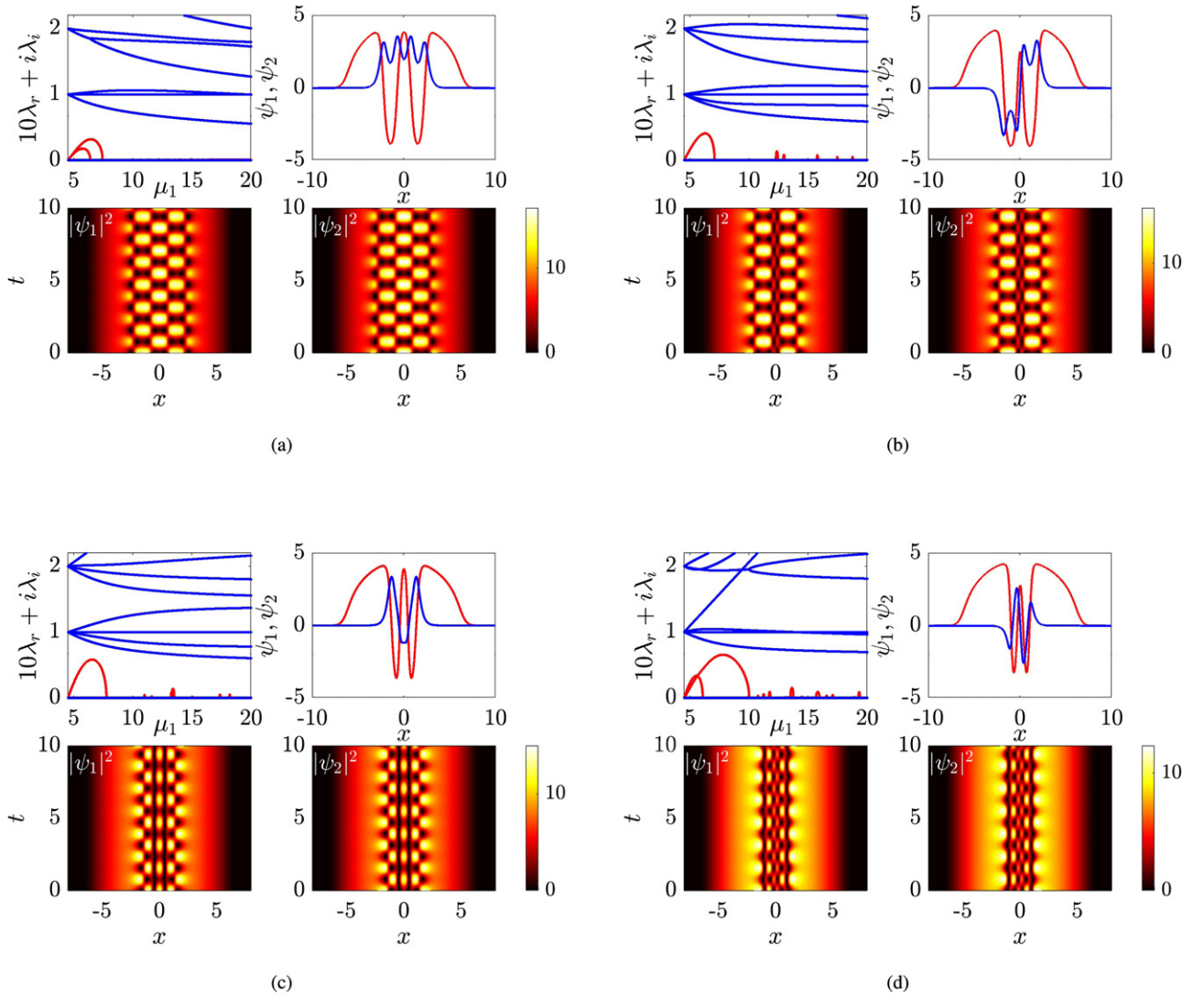


Figure 4. Same as figure 2, but for the \mathcal{S}_{4m} family of $m = 0$ (a), $m = 1$ (b), $m = 2$ (c), and $m = 3$ (d) from the linear limits $(4.5, m + 0.5)$ and up to a typical large-density limit $(20, 16)$ in the (μ_1, μ_2) parameter space. The top left quartet of panels concerns the \mathcal{S}_{40} state, the top right the \mathcal{S}_{41} configuration, while, respectively, the bottom left and right constitute the \mathcal{S}_{42} and \mathcal{S}_{43} states. In this case too, the initial conditions obtained as a result of the $SO(2)$ rotations lead to robust breathing states.

perspective, we can observe in the corresponding configurations that each of the DBs is converted, as a result of the

transformation, into a DD structure. On the other hand, a DD remains a DD when a collocated DD state exists, as in the case

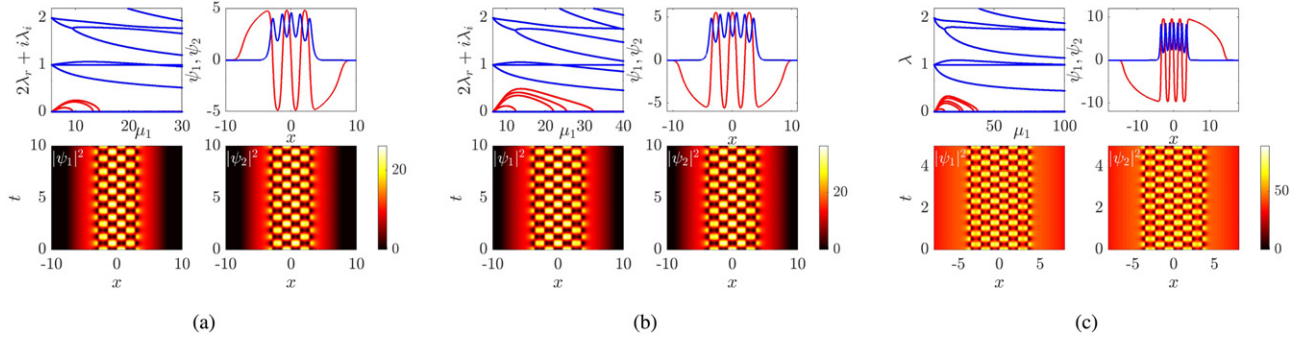


Figure 5. Same as figure 2, but for the S_{n0} states of $n = 5$ (a), $n = 6$ (b), and $n = 7$ (c) from the linear limits ($n + 0.5, 0.5$) to typical large-density limits. The final chemical potentials are (30, 25), (40, 35), (100, 88) for $n = 5, 6$, and 7 , respectively. Note that the number of unstable modes increases by 1 as n increases by 1.

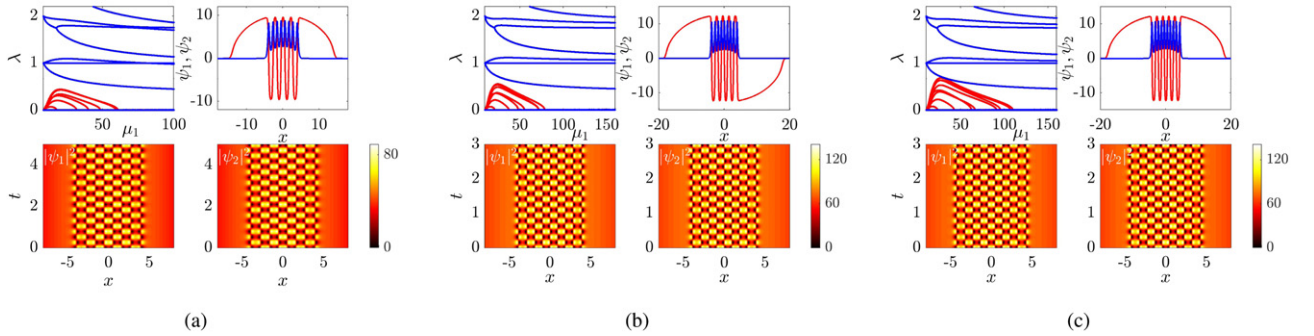


Figure 6. Same as figure 2, but for the S_{80} , S_{90} , and $S_{10,0}$ states of $n = 8$ (a), $n = 9$ (b), and $n = 10$ (c) from the linear limits to (100, 88), (160, 140), (160, 140), respectively. The number of unstable modes continues to grow by one as the number of dark solitons grows by one, upon examining the closely spaced unstable modes. Note that 10 DB solitons require as large as $\mu_1 \approx 100$ to be fully stabilized.

of S_{31} where the relevant zero crossing will be preserved even after the $SO(2)$ rotation. Similar features to the above ones can be detected for the S_{4m} family as shown in figure 4. Here, again the S_{40} state is the one that features the smallest number of instability bubbles, although it is relevant to note that off of the linear limit both the S_{40} and the S_{43} state feature two such bubbles (while S_{41} and S_{42} have only one associated instability). Nevertheless, all selected (spectrally) stable states at the DB level yield a number of stable internal vibrations upon $SO(2)$ rotating the former ones. This is demonstrated in the bottom sets of space-time contour plots within the figures 3 and 4.

Motivated by this observation, we next only look at S_{n0} states for $n = 5, 6, \dots, 10$. The results are presented in figures 5 and 6. Naturally, per the above observations, and in line with the results of [3], the number of unstable modes, stemming from the linear limits, increases by one whenever a dark soliton is added to the first component. This trend makes it challenging to stabilize multiple DB solitons. Indeed, for the $S_{10,0}$ state, we need chemical potentials of the order of 100 to fully stabilize this structure. However, for these sufficiently high values of the chemical potential, our direct numerical simulations confirm the presence of breathing rotated states with a large number of DD structures which lead to the corresponding internal vibrations and the associated breathing patterns. Since such initial conditions have been realized in the recent experiments of [23], it should, in principle, be possible to visualize and resolve the relevant dynamics.

The DD beating patterns have been obtained so far from perfectly stationary states; nevertheless, it is important to study the dynamics deviating from stationarity. In the parametric regime where a state is stable, it is expected that perturbations (such as initial speed) applied to it will remain bounded. This is confirmed through the following three examples. The various vibrational modes of states S_{10} (oscillation mode) and S_{20} (in-phase and out-of-phase oscillation modes) are excited by adding the corresponding BdG eigenvectors to the stationary solutions keeping the field norms unchanged. It is observed that the DD beating patterns remain robust existing on top of the above vibrations. In these dynamics, the internal excitation frequency is present and the dynamics is no longer a simple harmonic motion. It is also possible to set up intrinsic nonstationary states in the homogeneous setting where the trapping potential is absent. The appendix A has a collection of such analytical examples, ranging from nearly stationary ones (DB solitons seeded apart) to highly excited ones (DB solitons seeded much closer). It is interesting that these states can be spatially bounded and also exhibit several time scales in the beating dynamics, including the nearly stationary states.

Finally, we study the effects of weak deviations from the perfectly symmetric Manakov limit using the experimentally relevant values $g_{11} = 1.03$, $g_{22} = 0.97$, and $g_{12} = g_{21} = 1$ [15, 43]. In particular, figure 7 illustrates the breathing patterns corresponding to the S_{41} state, where the stable dynamics is suddenly subjected to the above interaction parameters

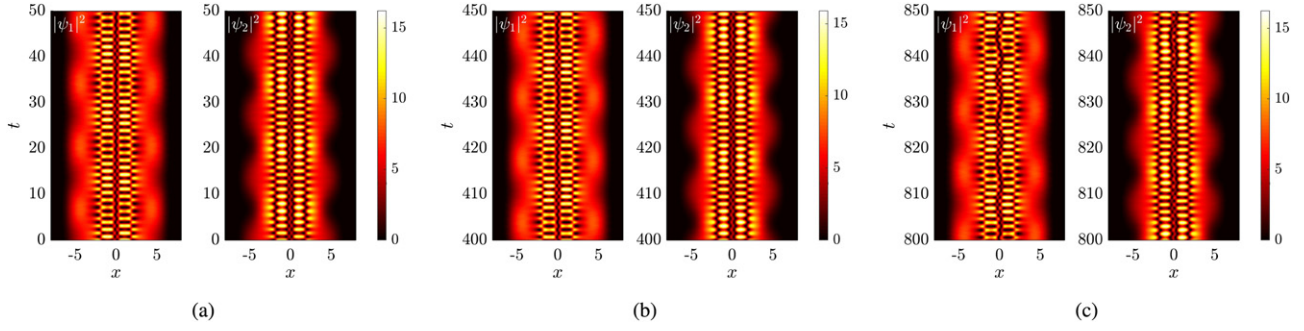


Figure 7. Weak disorder for few solitons caused by slight deviations from the perfectly symmetric Manakov limit using the experimentally relevant values $g_{11} = 1.03$, $g_{22} = 0.97$, and $g_{12} = g_{21} = 1$ [15]. Here, the breathing patterns emanating from the S_{41} state are illustrated, where the stable dynamics is suddenly subjected to the above interaction parameters starting from $t = 0$. Note that the ground state breathing mode is immediately excited, and the two condensates breathe in a correlated manner (a); see the boundary undulation of the condensates. The DD soliton breathing mode is finally also excited (around $t = 700$) and the breathing patterns become distorted. Nevertheless, the DD soliton breathing patterns remain robust (b) and (c) for several hundred periods before getting disordered.

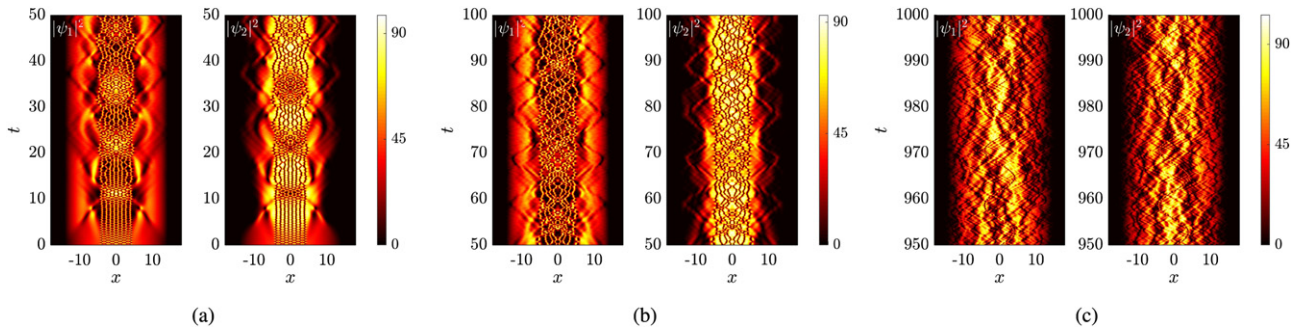


Figure 8. Same as figure 7 but for breathing patterns emanating from the S_{80} state. From about $t = 10$ onwards, the dark soliton ‘lattice’ gradually undergoes a transition towards a ‘gaseous’ state (a). In this state, the dark solitons frequently collide, thus generating dark bands in the density profiles. In addition, the background becomes highly excited and fragmented (b) and (c). See the text for more details.

starting from $t = 0$ (i.e. a quench to the above values of the interaction coefficients). Note that the ground state breathing mode is immediately excited, and the two condensates breathe in a correlated (out of phase) manner; see the relevant condensate boundaries. A DD soliton breathing mode is finally also excited (around $t = 700$) and the breathing patterns become distorted. Nevertheless, the soliton breathing patterns remain robust for several hundred periods before getting disordered. Similar behavior is found for other patterns, where some patterns persist for somewhat shorter periods (e.g. patterns resulting from S_{21} and S_{30}) and others remain robust for a much larger number of periods (e.g. patterns resulting from S_{31} and S_{40}).

Strong disorder can manifest quickly and in a pronounced manner for many solitons for the same parameters. A typical time evolution for the state S_{80} is shown in figure 8. In addition to the aforementioned weak disorder, the dark ‘lattice’ in each component can quickly evolve from a more ‘crystalline’ into a ‘gaseous’ state (in line with the terminology of [31]), where the synchronization of the DD soliton vibrations is gradually lost. The states then become so disordered that there is no clearly discernible stationary or periodic pattern. Indeed, dark solitons in the two components frequently collide forming some ‘dark bands’ in the density profile. The backgrounds of both states are also highly excited with this phenomenology

persisting up to the time horizon of the very long evolution simulations shown in figure 8.

3.2. Three-component dark–dark–dark (DDD) breathing patterns

In the last section of our present work, we turn our focus to the three-component case. In particular, the GPEs can be generalized to the following system:

$$i\frac{\partial\psi_1}{\partial t} = -\frac{1}{2}\frac{\partial^2\psi_1}{\partial x^2} + (g_{11}|\psi_1|^2 + g_{12}|\psi_2|^2 + g_{13}|\psi_3|^2)\psi_1 + V(x)\psi_1, \quad (8a)$$

$$i\frac{\partial\psi_2}{\partial t} = -\frac{1}{2}\frac{\partial^2\psi_2}{\partial x^2} + (g_{21}|\psi_1|^2 + g_{22}|\psi_2|^2 + g_{23}|\psi_3|^2)\psi_2 + V(x)\psi_2, \quad (8b)$$

$$i\frac{\partial\psi_3}{\partial t} = -\frac{1}{2}\frac{\partial^2\psi_3}{\partial x^2} + (g_{31}|\psi_1|^2 + g_{32}|\psi_2|^2 + g_{33}|\psi_3|^2)\psi_3 + V(x)\psi_3, \quad (8c)$$

where $\psi_j(x, t)$ ($j = 1, 2, 3$) are similarly the macroscopic wavefunctions and g_{ij} ($i, j = 1, 2, 3$) are the interaction coefficients with $g_{21} \equiv g_{12}$, $g_{31} \equiv g_{13}$, $g_{32} \equiv g_{23}$. Note that we will explore the Manakov case herein corresponding to $g_{ij} = 1$.

As discussed in the introduction, in addition to its mathematical interest, this scenario has been touched upon in nonlinear optical multi-component settings; a corresponding BEC framework would also need to incorporate the spin-dependent aspect of interactions within the spinor condensates [40, 41]. The Manakov setting features an SU(3) symmetry of the system. The external potential assumes the same parabolic form of $V(x) = (1/2)\omega^2 x^2$ with $\omega = 1$. Consequently, stationary states can be constructed by assuming

$$\psi_j(x, t) = \psi_j^0(x)e^{-i\mu_j t} \quad (9)$$

which transform equations (8a)–(8c) into the steady-state system:

$$-\frac{1}{2}\frac{d^2\psi_1^0}{dx^2} + (g_{11}|\psi_1^0|^2 + g_{12}|\psi_2^0|^2 + g_{13}|\psi_3^0|^2)\psi_1^0 + V(x)\psi_1^0 - \mu_1\psi_1^0 = 0, \quad (10a)$$

$$-\frac{1}{2}\frac{d^2\psi_2^0}{dx^2} + (g_{12}|\psi_1^0|^2 + g_{22}|\psi_2^0|^2 + g_{23}|\psi_3^0|^2)\psi_2^0 + V(x)\psi_2^0 - \mu_2\psi_2^0 = 0, \quad (10b)$$

$$-\frac{1}{2}\frac{d^2\psi_3^0}{dx^2} + (g_{13}|\psi_1^0|^2 + g_{23}|\psi_2^0|^2 + g_{33}|\psi_3^0|^2)\psi_3^0 + V(x)\psi_3^0 - \mu_3\psi_3^0 = 0, \quad (10c)$$

that we solve numerically. The computational set up is similar to the two-component case, tracing states from their linear limits to a TF regime. For completeness, the BdG stability analysis is presented in the appendix B. It is also relevant to mention that restricting this matrix to its 4×4 submatrix of the top left elements and setting $\psi_3 = 0$, one retrieves naturally as a special case the corresponding two-component BdG stability matrix. Since our goal is to illustrate the generality of our method, we will only examine in detail here two prototypical examples, namely the low-lying \mathcal{S}_{210} and \mathcal{S}_{310} states.

We perform the continuation of both states \mathcal{S}_{210} and \mathcal{S}_{310} over the chemical potentials from the associated linear limits to a TF regime of $(\mu_1, \mu_2, \mu_3) = (20, 18, 16)$. The left and right panels of figure 9 correspond to the BdG spectra of \mathcal{S}_{210} and \mathcal{S}_{310} , respectively. It should be noted that although both branches have intervals of instabilities (see the red colored, ‘instability bubbles’ in the pertinent panels), there exist *wide* intervals of stability where the solutions are expected to be long lived. Upon selecting stable steady states (according to our spectral stability analysis results), we SU(3)-rotate them in order to explore the possibility of forming breathing yet robust patterns in the three-component case. Generally, this can be done by means of a unitary matrix $U = e^{iH\theta}$, where H is a linear combination of the so-called Gell–Mann matrices [44]. To be more specific, we focus on a relatively symmetric rotation for simplicity (other ones and consequently other patterns are possible) dictated by the following unitary matrix [28]:

$$U = \frac{1}{\sqrt{3}} \begin{pmatrix} 1 & 1 & 1 \\ 1 & -\exp(i\pi/3) & \exp(i2\pi/3) \\ 1 & \exp(i2\pi/3) & -\exp(i\pi/3) \end{pmatrix}. \quad (11)$$

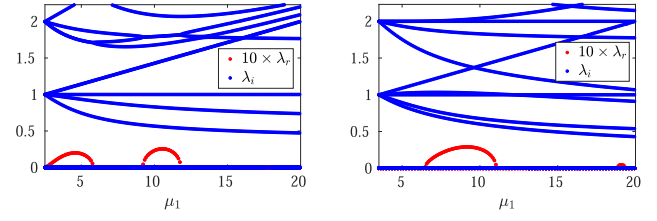


Figure 9. The BdG spectra ($\lambda = \lambda_r + i\lambda_i$) for the states \mathcal{S}_{210} (left) and \mathcal{S}_{310} (right) as a function of μ_1 . Here, the states emanate from the linear limits and our continuation terminates close to a TF regime with $(\mu_1, \mu_2, \mu_3) = (20, 18, 16)$. Note that both states feature wide intervals of stability. The real parts in both panels are multiplied by a factor of 10 for visualization purposes.

Figures 10 and 11 summarize our results for the \mathcal{S}_{210} and \mathcal{S}_{310} , respectively. In particular, the top panels therein showcase the spatial distribution of the densities of the respective components for the unrotated (dashed-dotted lines) and rotated (solid lines) solutions. The bottom panels in the figures offer the spatio-temporal evolution of the subsequent dark–dark–dark (DDD) beating patterns ($|\psi_1(x, t)|^2$, $|\psi_2(x, t)|^2$, and $|\psi_3(x, t)|^2$ are shown from left to right). Naturally, there are two dark solitons in each component for the rotated \mathcal{S}_{210} whereas there exist three for the rotated \mathcal{S}_{310} . The beating dynamics of \mathcal{S}_{210} is robustly periodic, featuring a single-period internal vibration of the state. Upon examination, this is a coincidence resulting from our chosen parameters, where $\mu_1 - \mu_2 = \mu_2 - \mu_3$, yielding only one period, i.e. $2\pi/(\mu_1 - \mu_2) \approx 3.6664$. This agrees very well with the results of our simulations. On the other hand, two frequencies are genuinely present for the \mathcal{S}_{310} beating dynamics, as the above relation has not been selected in our initial data. Beating patterns for the \mathcal{S}_{210} state in the homogeneous setting, i.e. without an external trapping potential, were studied analytically for particular solutions [28]. However, in the present work, we demonstrate that this state exists and is, in fact, robust over a wide range of parameters.

Here, we summarize the key findings of this section for both two-component and three-component systems:

- We have systematically constructed a series of complex, stationary and breathing soliton states from their bifurcating linear limits to the TF regimes in both two- and three-component systems, and find that they can all feature wide parametric intervals of stability in the TF regimes for the solitons considered herein.
- The two-component stationary soliton \mathcal{S}_{nm} produces n DD beating patterns after applying a unitary rotation to the former. The pattern gets increasingly in phase as m increases from 0 to $n - 1$.
- The three-component stationary soliton \mathcal{S}_{nmp} after unitary rotation produces DDD beating patterns. These patterns are typically more complex with multiple frequencies present in the oscillation dynamics.
- The above beating patterns are robust and observable if the starting point (prior to rotation) consists of a dynamically stable state. This is so even if the stable initial

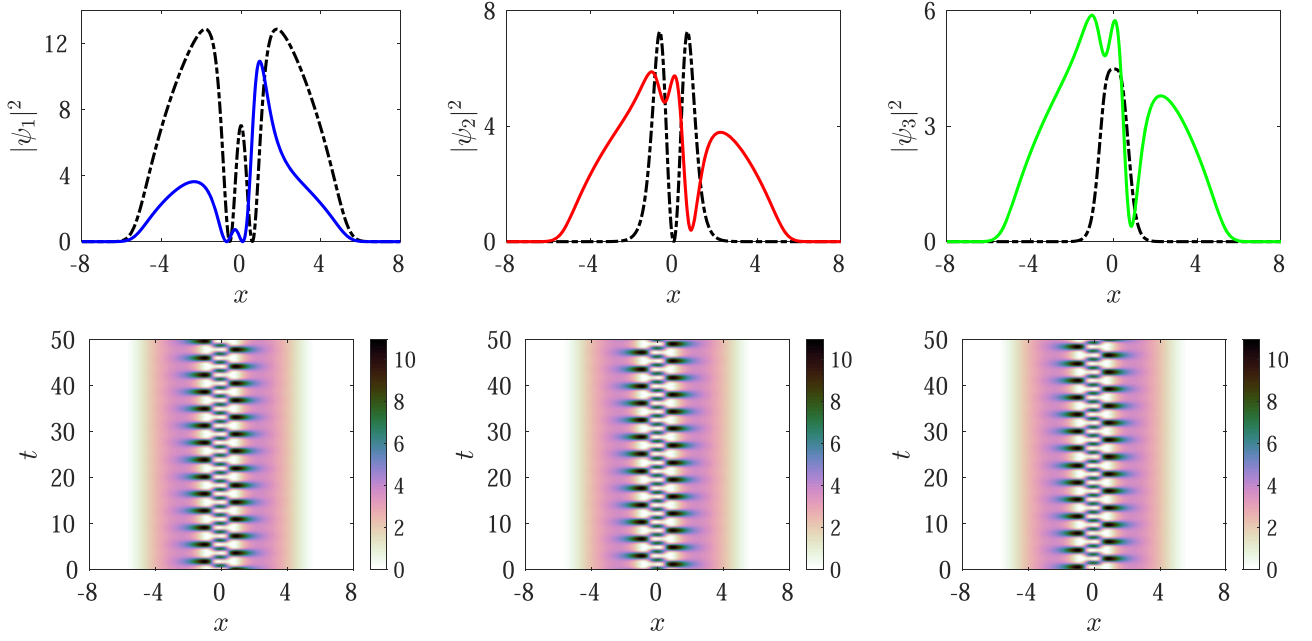


Figure 10. Summary of results for the \mathcal{S}_{210} state. *Top row:* the densities $|\psi_j|^2$ ($j = 1, 2, 3$) of the steady-state profiles for $\mu_1 = 14.998\,146$, $\mu_2 = 13.284\,432$, and $\mu_3 = 11.570\,432$ are shown with dashed-dotted black lines, and the SU(3) rotated versions of them are shown with solid blue, red, and green lines, respectively. *Bottom row:* spatio-temporal evolutions of the densities $|\psi_1(x, t)|^2$ (left panel), $|\psi_2(x, t)|^2$ (middle panel), and $|\psi_3(x, t)|^2$ (right panel) are shown where the initial states employed are the SU(3) rotated states of the top row.

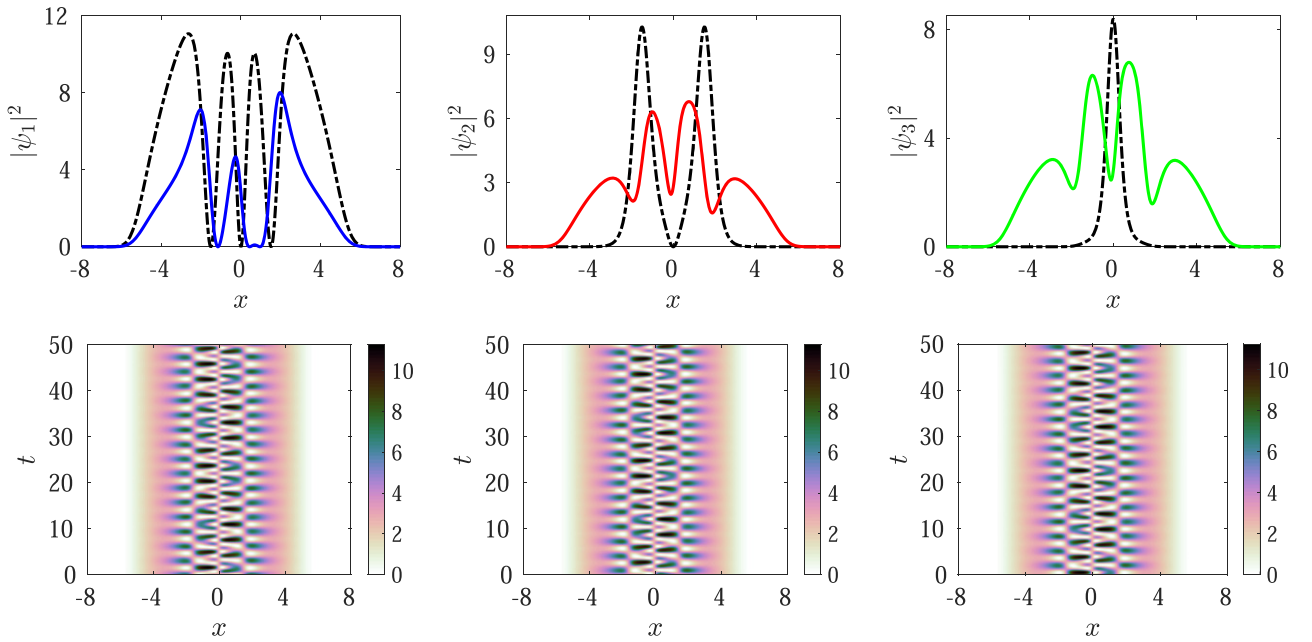


Figure 11. Same as figure 10 but for the \mathcal{S}_{310} state with chemical potentials $\mu_1 = 15.283\,574$, $\mu_2 = 13.283\,574$, and $\mu_3 = 11.569\,574$. Note that there are genuinely two frequencies involved in this DDD breathing dynamics.

stationary state is perturbed before rotation, or interaction parameters deviate slightly from the Manakov limit.

Finally, these beating dynamics should be readily accessible experimentally, e.g. in hyperfine states of ^{87}Rb condensates, given the substantial recent developments in manipulating cold atoms. In particular, DD (or DDD in the three-component counterpart) solitons may be directly generated in condensate counterflow experiments [45]. Alternatively, it

should be possible to first prepare, e.g. DB structures in a controlled manner using combined density and phase engineering [32, 46, 47] and subsequently rotate to DD structures using Rabi oscillations [48] and the spatially dependent control thereof that has been recently used experimentally to create multi-soliton patterns [23]. It should also be noted that the recent work of [33] that appeared after the submission of the present work offered another example of the type of control that is available presently with multi-component solitons.

The utilization of spatially dependent spin rotations realized via steerable laser beams enables the local coherent transfer of atoms across components and the controlled creation of dark–bright–bright solitons with arbitrary phases so as to examine their collisions. These techniques and their local density and phase control are strongly suggestive that the types of dynamically robust patterns proposed herein should be experimentally accessible. Indeed, the work of [33] is important for yet another reason, namely that it realized for the first time experimentally the three-component model with equal density-dependent interactions, i.e. the three-component Manakov model, that we also touch upon herein.

4. Conclusions and future challenges

The present work offered a systematic study of distinct $SO(2)$ -induced multiple DD breathing patterns from stationary and stable DB and DD bound modes. In particular, we studied the existence and stability of these structures from their respective linear limits to typical TF regimes, where they are found to possess wide parametric intervals of spectral stability. We found that for n solitons, there are n distinct coherent patterns that stem from the linear limit and which range from fully in-phase to fully out-of-phase ones. Analytical results in the homogeneous setting are also discussed: here the rotation typically involves the breathing of dynamically non-stationary configurations. Moreover, we presented a generalization of our approach to the three-component GPE system to illustrate prototypical case examples showcasing the generality of the considerations discussed herein.

Motivated by this work, there are multiple avenues for future study that we plan to pursue. One natural extension of our work is to generalize considerations to higher dimensions. In 2D, vortex clusters and/or dark soliton filaments filled with bright components of various relative phases are possible, generating, e.g. various vortex cluster-vortex cluster breathing patterns. In 3D, vortex filaments and/or dark soliton surfaces filled with bright components of various relative phases are relevant for future studies. Importantly, recent experimental progress, including, e.g. the configurations reported in [23], suggests that such states can be accessed as initial conditions in state-of-the-art experiments and hence the corresponding vibrational dynamics should, in principle, be experimentally tractable. It is not readily obvious that one can find a systematic way to construct all the topologically distinct states and breathing patterns as in 1D since new states can bifurcate away from the linear limit [49]. In addition, there are also different possible combinations of linear eigenmodes. For instance, $|1, 0\rangle$ (where the separated by comma indices denote here the linear eigenstates in the different spatial dimensions) produces a dark soliton stripe, while $(|1, 0\rangle + i|0, 1\rangle)/\sqrt{2}$ produces a single vortex, starting from essentially the same basis. An additional challenge concerns the (in)stability properties of these structures. It is relevant to seek suitable potential configurations to stabilize, e.g. some dark soliton filaments and surfaces against their transverse instabilities by adding external pinning potentials. It is also challenging to stabilize certain multiple vortical filament structures, and preliminary data suggest that

even the double vortex rings filled by either in-phase or out-of-phase bright components are extremely difficult to stabilize, at least in a spherical trap. In this situation, one can either further increase the chemical potentials or explore instead other trap settings.

Finally, systematic studies of the three-component system and even beyond that are also interesting; notice, in that vein, both the $F = 1$ and $F = 2$ spinor systems are presently experimentally accessible in atomic condensates [40, 41]. In our work, we have studied a few selected examples of three-component structures, focusing, in particular, on the Manakov case. Yet, more complex structures should be accessible under physically realistic (spinor) perturbations, but also in higher dimensions. Research work along these lines are currently in progress, and will be reported in future publications.

Acknowledgments

WW acknowledges support from National Science Foundation of China under Grant No. 12004268, and the Fundamental Research Funds for the Central Universities, China. This work is supported by National Natural Science Foundation of China (Contact No. 11775176), Basic Research Program of Natural Science of Shaanxi Province (Grant No. 2018KJXX-094), The Key Innovative Research Team of Quantum Many-Body Theory and Quantum Control in Shaanxi Province (Grant No. 2017KCT-12), and the Major Basic Research Program of Natural Science of Shaanxi Province (Grant No. 2017ZDJC-32). PGK acknowledges support from the US National Science Foundation under Grant Nos. PHY-1602994 and DMS-1809074. He also acknowledges support from the Leverhulme Trust via a Visiting Fellowship and the Mathematical Institute of the University of Oxford for its hospitality during part of this work. We thank the Emei cluster at Sichuan university for providing HPC resources.

Data availability statement

The data that support the findings of this study are available upon reasonable request from the authors.

Appendix A. Multiple dark–dark soliton breathing patterns in a homogeneous setting

The multi-DB solutions here are calculated using a modified Darboux transformation in the homogeneous setting [50]. Two typical quasi-static solutions along with the symmetric $SO(2)$ rotated solutions are depicted in figure 12 where the panel (a) of the figure shows the evolution of two well-separated DB solitons; essentially these waves are sufficiently far away from each other and, hence, do not feel the presence of each other over the time scale of the simulation. As a result, over the horizon of the simulation shown in panel (a) of figure 12, the internal beating of each of the two DD solitary waves occurs with different frequencies. When the solitons are initialized closer, the interaction between them affects the beating patterns as illustrated in figure 12(b). Similarly, the cases for three

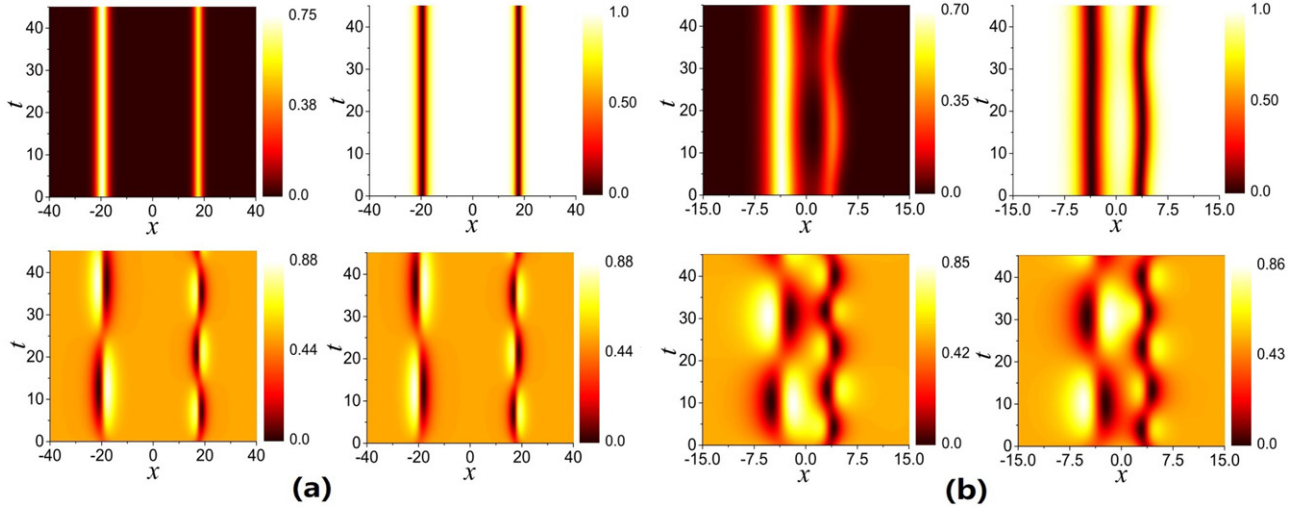


Figure 12. Space-time density evolutions of two DB solitons and DD breathing patterns for well-separated (a) and closely initialized (b) cases. The top panels show the bright-soliton component and the dark-soliton component, and the lower panels show the rotated DD breathing patterns. The well-separated solitons yield effectively isolated beating DD solitons, while the nonlinear interaction between solitons changes the beating patterns significantly.

DB solutions and the rotated dynamics are shown in figure 13. Figure 13(a) shows the evolution of three well-separated DB solitons, again with very distinct breathing frequencies. As the initial DBs are brought closer, the beating patterns again become strongly affected by the interaction between solitons; cf figure 12(b). These beating patterns are found to be stable against weak perturbations. The resulting pattern being highly evolving over time remains spatially localized. Note, however, that this would no longer be true in the attractive case [51] due to modulational instability of the (density) background.

Appendix B. Linear stability analysis of the three-component GPE

Upon substituting equation (7) (with $j = 1, 2, 3$) into equations (8a)–(8c), we obtain at order $O(\varepsilon)$ an eigenvalue problem of the form:

$$\rho \begin{pmatrix} a_1 \\ b_1 \\ a_2 \\ b_2 \\ a_3 \\ b_3 \end{pmatrix} = \begin{pmatrix} A_{11} & A_{12} & A_{13} & A_{14} & A_{15} & A_{16} \\ -A_{12}^* & -A_{11} & -A_{14}^* & -A_{13}^* & -A_{16}^* & -A_{15}^* \\ A_{13}^* & A_{14} & A_{33} & A_{34} & A_{35} & A_{36} \\ -A_{14}^* & -A_{13} & -A_{34}^* & -A_{33} & -A_{36}^* & -A_{35}^* \\ A_{15}^* & A_{16} & A_{35}^* & A_{36} & A_{55} & A_{56} \\ -A_{16}^* & -A_{15} & -A_{36}^* & -A_{35} & -A_{56}^* & -A_{55}^* \end{pmatrix} \times \begin{pmatrix} a_1 \\ b_1 \\ a_2 \\ b_2 \\ a_3 \\ b_3 \end{pmatrix}, \quad (12)$$

where the distinct matrix elements are given by:

$$\begin{aligned} A_{11} &= -\frac{1}{2} \frac{d^2}{dx^2} + 2g_{11}|\psi_1^0|^2 + g_{12}|\psi_2^0|^2 + g_{13}|\psi_3^0|^2 + V(x) - \mu_1, \\ A_{12} &= g_{11}(\psi_1^0)^2, \\ A_{13} &= g_{12}\psi_1^0(\psi_2^0)^*, \\ A_{14} &= g_{12}\psi_1^0\psi_2^0, \\ A_{15} &= g_{13}\psi_1^0(\psi_3^0)^*, \\ A_{16} &= g_{13}\psi_1^0\psi_3^0, \\ A_{33} &= -\frac{1}{2} \frac{d^2}{dx^2} + g_{12}|\psi_1^0|^2 + 2g_{22}|\psi_2^0|^2 + g_{23}|\psi_3^0|^2 + V(x) - \mu_2, \\ A_{34} &= g_{22}(\psi_2^0)^2, \\ A_{35} &= g_{23}\psi_2^0(\psi_3^0)^*, \\ A_{36} &= g_{23}\psi_2^0\psi_3^0, \\ A_{55} &= -\frac{1}{2} \frac{d^2}{dx^2} + g_{13}|\psi_1^0|^2 + g_{23}|\psi_2^0|^2 + 2g_{33}|\psi_3^0|^2 + V(x) - \mu_3, \\ A_{56} &= g_{33}(\psi_3^0)^2. \end{aligned}$$

Here, $\rho = i\lambda$ is the eigenvalue with the associated eigenvector:

$$\mathbf{W}(x) = (a_1(x)b_1(x)a_2(x)b_2(x)a_3(x)b_3(x))^T.$$

The eigenvalue computations for the three-component case were performed by using the FEAST eigenvalue solver [52] where (usually) 100 eigenvalues were computed with 10^{-8} tolerance on the residuals.

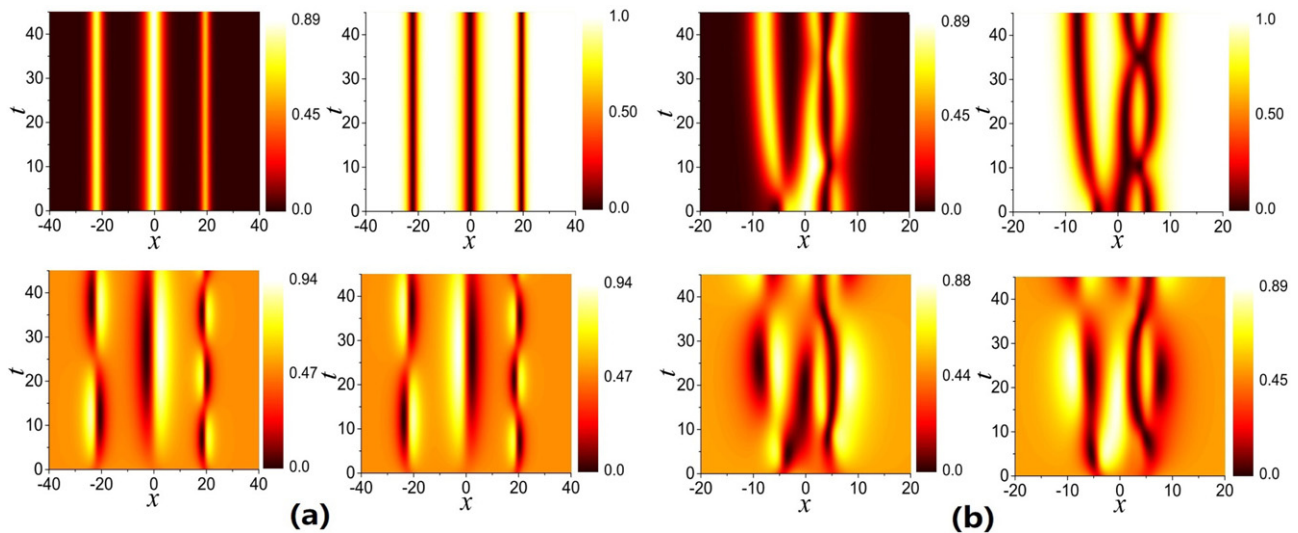


Figure 13. Similar to the previous figure but now for the three DB soliton case, once again when well-separated (a) and nonlinearly interacting (b).

ORCID iDs

Wenlong Wang <https://orcid.org/0000-0001-5980-3236>

Efstathios G Charalampidis <https://orcid.org/0000-0002-5417-4431>

Panayotis G Kevrekidis <https://orcid.org/0000-0002-7714-3689>

References

- [1] Pitaevskii L and Stringari S 2003 *Bose–Einstein Condensation* (Oxford: Oxford University Press)
- [2] Pethick C and Smith H 2002 *Bose–Einstein Condensation in Dilute Gases* (Cambridge: Cambridge University Press)
- [3] Kevrekidis P G, Frantzeskakis D J and Carretero-González R 2015 *The Defocusing Nonlinear Schrödinger Equation: From Dark Solitons to Vortices and Vortex Rings* (Philadelphia, PA: SIAM)
- [4] Kivshar Y and Luther-Davies B 1998 Dark optical solitons: physics and applications *Phys. Rep.* **298** 81
- [5] Abdullaev F, Gammal A, Kamchatnov A and Tomio L 2005 Dynamics of bright matter wave solitons in a Bose–Einstein condensate *Int. J. Mod. Phys. B* **19** 3415
- [6] Frantzeskakis D J 2010 Dark solitons in atomic Bose–Einstein condensates: from theory to experiments *J. Phys. A: Math. Theor.* **43** 213001
- [7] Fetter A L and Svidzinsky A A 2001 Vortices in a trapped dilute Bose–Einstein condensate *J. Phys.: Condens. Matter* **13** R135
- [8] Fetter A L 2009 Rotating trapped Bose–Einstein condensates *Rev. Mod. Phys.* **81** 647
- [9] Komineas S 2007 Vortex rings and solitary waves in trapped Bose–Einstein condensates *Eur. Phys. J. Spec. Top.* **147** 133
- [10] Proment D, Onorato M and Barenghi C F 2012 Vortex knots in a Bose–Einstein condensate *Phys. Rev. E* **85** 036306
- [11] Busch T and Anglin J R 2001 Dark–bright solitons in inhomogeneous Bose–Einstein condensates *Phys. Rev. Lett.* **87** 010401
- [12] Becker C, Stellmer S, Soltan-Panahi P, Dörscher S, Baumert M, Richter E-M, Kronjäger J, Bongs K and Sengstock K 2008 Oscillations and interactions of dark and dark–bright solitons in Bose–Einstein condensates *Nat. Phys.* **4** 496
- [13] Romero-Ros A, Katsimiga G C, Kevrekidis P G and Schmelcher P 2019 Controlled generation of dark–bright soliton complexes in two-component and spinor Bose–Einstein condensates *Phys. Rev. A* **100** 013626
- [14] Kiehn H, Mistakidis S I, Katsimiga G C and Schmelcher P 2019 Spontaneous generation of dark–bright and dark–antidark solitons upon quenching a particle-imbalanced bosonic mixture *Phys. Rev. A* **100** 023613
- [15] Yan D, Chang J J, Hamner C, Kevrekidis P G, Engels P, Achilleos V, Frantzeskakis D J, Carretero-González R and Schmelcher P 2011 Multiple dark–bright solitons in atomic Bose–Einstein condensates *Phys. Rev. A* **84** 053630
- [16] Kevrekidis P G and Frantzeskakis D J 2016 Solitons in coupled nonlinear Schrödinger models: a survey of recent developments *Rev. Phys.* **1** 140
- [17] Wang W and Kevrekidis P G 2017 Two-component dark–bright solitons in three-dimensional atomic Bose–Einstein condensates *Phys. Rev. E* **95** 032201
- [18] Kevrekidis P G, Wang W, Carretero-González R and Frantzeskakis D J 2018 Adiabatic invariant analysis of dark and dark–bright soliton stripes in two-dimensional Bose–Einstein condensates *Phys. Rev. A* **97** 063604
- [19] Wang W, Kevrekidis P G and Babaev E 2019 Ring dark solitons in three-dimensional Bose–Einstein condensates *Phys. Rev. A* **100** 053621
- [20] Bersano T M, Gokhroo V, Khamsehchi M A, D’Ambroise J, Frantzeskakis D J, Engels P and Kevrekidis P G 2018 Three-component soliton states in spinor $F = 1$ Bose–Einstein condensates *Phys. Rev. Lett.* **120** 063202
- [21] Qu C, Pitaevskii L P and Stringari S 2016 Magnetic solitons in a binary Bose–Einstein condensate *Phys. Rev. Lett.* **116** 160402
- [22] Chai X, Lao D, Fujimoto K, Hamazaki R, Ueda M and Raman C 2020 Magnetic solitons in a spin-1 Bose–Einstein condensate *Phys. Rev. Lett.* **125** 030402
- [23] Katsimiga G C, Mistakidis S I, Bersano T M, Ome M K H, Mossman S M, Mukherjee K, Schmelcher P, Engels P and Kevrekidis P G 2020 Observation and analysis of multiple dark–antidark solitons in two-component Bose–Einstein condensates *Phys. Rev. A* **102** 023301

- [24] Manakov S V 1974 On the theory of two-dimensional stationary self-focusing of electromagnetic waves *Sov. Phys - JETP* **38** 248
- [25] Park Q-H and Shin H 2000 Systematic construction of multi-component optical solitons *Phys. Rev. E* **61** 3093
- [26] Yan D, Chang J J, Hamner C, Hofer M, Kevrekidis P G, Engels P, Achilleos V, Frantzeskakis D J and Cuevas J 2012 Beating dark–dark solitons in Bose–Einstein condensates *J. Phys. B: At. Mol. Opt. Phys.* **45** 115301
- [27] Charalampidis E G, Wang W, Kevrekidis P G, Frantzeskakis D J and Cuevas-Maraver J 2016 SO(2)-induced breathing patterns in multicomponent Bose–Einstein condensates *Phys. Rev. A* **93** 063623
- [28] Zhao L-C 2018 Beating effects of vector solitons in Bose–Einstein condensates *Phys. Rev. E* **97** 062201
- [29] Ohta Y, Wang D-S and Yang J 2011 General N -dark–dark solitons in the coupled nonlinear Schrödinger equations *Stud. Appl. Math.* **127** 345
- [30] de O Assunção A, Blas H and da Silva M J B F 2012 New derivation of soliton solutions to the AKNS₂ system via dressing transformation methods *J. Phys. A: Math. Theor.* **45** 085205
- [31] Wang W and Kevrekidis P G 2015 Transitions from order to disorder in multiple dark and multiple dark–bright soliton atomic clouds *Phys. Rev. E* **91** 032905
- [32] Fritsch A R, Lu M, Reid G H, Piñeiro A M and Spielman I B 2020 Creating solitons with controllable and near-zero velocity in Bose–Einstein condensates *Phys. Rev. A* **101** 053629
- [33] Lannig S, Schmied C-M, Prüfer M, Kunkel P, Strohmaier R, Strobel H, Gasenzer T, Kevrekidis P G and Oberthaler M K 2020 Collisions of three-component vector solitons in Bose–Einstein condensates *Phys. Rev. Lett.* **125** 170401
- [34] Atkinson K E 1989 *An Introduction to Numerical Analysis* (New York: Wiley)
- [35] Coles M P, Pelinovsky D E and Kevrekidis P G 2010 Excited states in the large density limit: a variational approach *Nonlinearity* **23** 1753
- [36] Cohen-Tannoudji C, Diu B and Laloë F 1977 *Quantum Mechanics (Trans. of: Mécanique Quantique. Paris: Hermann, 1973)* (New York: Wiley)
- [37] Görlitz A et al 2001 Realization of Bose–Einstein condensates in lower dimensions *Phys. Rev. Lett.* **87** 130402
- [38] Weller A, Ronzheimer J P, Gross C, Esteve J, Oberthaler M K, Frantzeskakis D J, Theocharis G and Kevrekidis P G 2008 Experimental observation of oscillating and interacting matter wave dark solitons *Phys. Rev. Lett.* **101** 130401
- [39] Gaunt A L, Schmidutz T F, Gotlibovych I, Smith R P and Hadzibabic Z 2013 Bose–Einstein condensation of atoms in a uniform potential *Phys. Rev. Lett.* **110** 200406
- [40] Kawaguchi Y and Ueda M 2012 Spinor Bose–Einstein condensates *Phys. Rep.* **520** 253
- [41] Stamper-Kurn D M and Ueda M 2013 Spinor Bose gases: symmetries, magnetism, and quantum dynamics *Rev. Mod. Phys.* **85** 1191
- [42] Ostrovskaya E A, Kivshar Y S, Chen Z and Segev M 1999 Interaction between vector solitons and solitonic gluons *Opt. Lett.* **24** 327
- [43] Mertes K M, Merrill J W, Carretero-González R, Frantzeskakis D J, Kevrekidis P G and Hall D S 2007 Nonequilibrium dynamics and superfluid ring excitations in binary Bose–Einstein condensates *Phys. Rev. Lett.* **99** 190402
- [44] Gell-Mann M 1962 Symmetries of baryons and mesons *Phys. Rev.* **125** 1067
- [45] Hamner C, Chang J J, Engels P and Hofer M A 2011 Generation of dark–bright soliton trains in superfluid–superfluid counterflow *Phys. Rev. Lett.* **106** 065302
- [46] Williams J E and Holland M J 1999 Preparing topological states of a Bose–Einstein condensate *Nature* **401** 568
- [47] Carr L D, Brand J, Burger S and Sanpera A 2001 Dark-soliton creation in Bose–Einstein condensates *Phys. Rev. A* **63** 051601
- [48] Nistazakis H E, Rapti Z, Frantzeskakis D J, Kevrekidis P G, Sodano P and Trombettoni A 2008 Rabi switch of condensate wave functions in a multicomponent Bose gas *Phys. Rev. A* **78** 023635
- [49] Charalampidis E G, Boullé N, Farrell P E and Kevrekidis P G 2020 Bifurcation analysis of stationary solutions of two-dimensional coupled Gross–Pitaevskii equations using deflated continuation *Commun. Nonlinear Sci. Numer. Simul.* **87** 105255
- [50] Ling L, Zhao L-C and Guo B 2015 Darboux transformation and multi-dark soliton for N -component nonlinear Schrödinger equations *Nonlinearity* **28** 3243
- [51] Zhao L-C, Duan L, Gao P and Yang Z-Y 2019 Vector rogue waves on a double-plane wave background *Europhys. Lett.* **125** 40003
- [52] Kestyn J, Polizzi E and Tang T P 2016 Feast eigensolver for non-Hermitian problems *SIAM J. Sci. Comput.* **38** S772